Rapid Communications

Influence of the neutron-skin effect on nuclear isobar collisions at energies available at the BNL Relativistic Heavy Ion Collider

Jan Hammelmann,[1,2,*] Alba Soto-Ontoso,[3,†] Massimiliano Alvioli,[4,5,‡] Hannah Elfner,[1,2,6,§] and Mark Strikman[7,∥]

[1]*Goethe-Universität Frankfurt, Max-von-Laue-Strasse 1, 60438 Frankfurt am Main, Germany*
[2]*Frankfurt Institute for Advanced Studies, Ruth-Moufang-Strasse 1, 60438 Frankfurt am Main, Germany*
[3]*Physics Department, Brookhaven National Laboratory, Upton, New York 11973, USA*
[4]*Consiglio Nazionale delle Ricerche, Istituto di Ricerca per la Protezione Idrogeologica, via Madonna Alta 126, I-06128 Perugia, Italy*
[5]*Istituto Nazionale di Fisica Nucleare, Sezione di Perugia, Via A. Pascoli, I-06123, Perugia, Italy*
[6]*GSI Helmholtzzentrum für Schwerionenforschung GmbH, Planckstrasse 1, 64291 Darmstadt, Germany*
[7]*Physics Department, Pennsylvania State University, University Park, Pennsylvania 16802, USA*

(Received 25 October 2019; revised manuscript received 20 March 2020; accepted 26 May 2020; published 30 June 2020)

The unambiguous observation of a chiral magnetic effect (CME)–driven charge separation is the core aim of the isobar program at the Relativistic Heavy Ion Collider (RHIC), consisting of $^{96}_{40}$Zr + $^{96}_{40}$Zr and $^{96}_{44}$Ru + $^{96}_{44}$Ru collisions at $\sqrt{s_{\rm NN}} = 200$ GeV. We quantify the role of the spatial distributions of the nucleons in the isobars on both eccentricity and magnetic field strength within a relativistic hadronic transport approach (simulating many accelerated strongly interacting hadrons, SMASH). In particular, we introduce isospin-dependent nucleon-nucleon spatial correlations in the geometric description of both nuclei, deformation for $^{96}_{44}$Ru and the so-called neutron skin effect for the neutron-rich isobar, i.e., $^{96}_{40}$Zr. The main result of this study is a reduction of the magnetic field strength difference between $^{96}_{44}$Ru + $^{96}_{44}$Ru and $^{96}_{40}$Zr + $^{96}_{40}$Zr by a factor of 2, from 10% to 5% in peripheral collisions when the neutron-skin effect is included. Further, we find an increase of the eccentricity ratio between the isobars by up to 10% in ultracentral collisions as due to the deformation of $^{96}_{44}$Ru while neither the neutron skin effect nor the nucleon-nucleon correlations result into a significant modification of this observable with respect to the traditional Woods-Saxon modeling. Our results suggest a significantly smaller CME signal to background ratio for the experimental charge separation measurement in peripheral collisions with the isobar systems than previously expected.

DOI: 10.1103/PhysRevC.101.061901

Introduction. One of the fundamental properties of quantum chromodynamics (QCD) is the axial anomaly, which in the massless fermion limit reads as follows:

$$\partial_\mu j_5^\mu = -\frac{g^2}{16\pi^2} F^a_{\mu\nu}\widetilde{F}^{a,\mu\nu}, \tag{1}$$

where $F^a_{\mu\nu}$ is the gluon field strength, $\widetilde{F}^{a,\mu\nu}$ is its dual, g is the strong coupling constant, and j_5^μ is the axial current density. The axial anomaly establishes a direct relationship between the generation of a net axial charge and the dynamics of non-Abelian gauge fields.

Together with condensed matter systems [1], ultrarelativistic heavy-ion collisions provide a unique environment to experimentally test the chiral anomaly. At least two mechanisms contribute to the right-hand side of Eq. (1). On the one hand, in the color glass condensate description of the early, nonequilibrium stage of the collision known as glasma [2], fluctuations of the chromoelectric and chromomagnetic fields give rise to a nonvanishing $F^a_{\mu\nu}\widetilde{F}^{a,\mu\nu}$ [3,4]. Further, the nontrivial topological structure of the QCD vacuum results into another source of net axial charge density known as sphaleron transitions, whose rate is enhanced at high temperatures such as the ones reached in the quark-gluon plasma phase [5–7]. These local fluctuations of axial charge density in the transverse plane occur in the presence of a strong electromagnetic field in noncentral collisions [8,9]. Then, the chiral imbalance is efficiently converted into a separation of positive and negative charges along the direction of the magnetic field. This phenomenon, dubbed chiral magnetic effect (CME) [10,11], manifests itself into charge-dependent azimuthal correlations of the measured hadrons [12].

A decade after the pioneering analysis of the STAR Collaboration [13], the experimental confirmation of the CME remains unsettled. Numerous charge separation measurements in line with CME expectations were reported with different collisions systems and energies both from the Relativisitic Heavy Ion Collider (RHIC) [14–16] and the Large Hadron Collider (LHC) [17,18]. However, these measurements are known to be strongly affected by background contamination

*hammelmann@fias.uni-frankfurt.de
†ontoso@bnl.gov
‡massimiliano.alvioli@irpi.cnr.it
§elfner@fias.uni-frankfurt.de
∥mxs43@psu.edu

arising from flow [19] and local charge conservation [20]. Observables beyond the traditional three-particle correlator could help solve the problem [21]. Moreover, RHIC measurements with different isobars, i.e., ${}^{96}_{40}$Zr and ${}^{96}_{44}$R [22], could disentangle the background from the signal. For that purpose, ${}^{96}_{40}\mathrm{Zr} + {}^{96}_{40}\mathrm{Zr}$ collisions will provide a precise characterization of the background contribution to the experimental charge separation measurement. On the other hand, the proton-rich isobar system ${}^{96}_{44}\mathrm{Ru} + {}^{96}_{44}\mathrm{Ru}$ will provide an enhanced sensitivity to the CME component, due to the formation of larger magnetic fields.

A correct interpretation of the forthcoming experimental data requires accurate quantification of background and signal from theory. A multiphase transport model predicted the magnetic field strength, proportional to the CME contribution, to be 10% larger for ${}^{96}_{44}\mathrm{Ru} + {}^{96}_{44}\mathrm{Ru}$ than for ${}^{96}_{40}\mathrm{Zr} + {}^{96}_{40}\mathrm{Zr}$ in peripheral collisions [23,24]. A hydrodynamic framework predicted differences of up to 10% on the elliptic flow of both collision systems related to deformation [25]. A systematic comparison between a Woods-Saxon shape and density functional theory calculations shows that the functional form of the nuclear density distributions used in the simulations also impacts v_2 ($\approx$3%) [26]. All in all, the results of these studies identify the nuclear structure of the two-isobar nuclei to be a source of uncertainty for v_2 but not for the magnetic field strength.

In this work, we analyze the effect due to an experimentally measured nuclear phenomenon in the description of the density distribution of ${}^{96}_{40}$Zr, i.e., the neutron-skin effect [27,28]. This ingredient leads to an enhancement of the magnetic field in peripheral ${}^{96}_{40}\mathrm{Zr} + {}^{96}_{40}\mathrm{Zr}$ collisions within SMASH [29] consequently undermining the experimental prospects of finding out the chiral magnetic effect with the isobar run.

Neutron-skin effect and nucleon-nucleon correlations. Traditionally, the spatial distribution of nucleons inside nuclei is generated by randomly sampling the Woods-Saxon density distribution [30]

$$\rho(r,\theta) = \frac{\rho_0}{e^{(r-R'(\theta,\phi))/d} + 1}, \tag{2}$$

where

$$R'(\theta) = R_0(1 + \beta_2 Y_2^0(\theta)). \tag{3}$$

In Eqs. (2) and (3), $\rho_0 = 0.168$ is the ground-state density, d refers to the difussiveness, R_0 is the nuclear radius, and β_2 together with the spherical harmonic Y_2^0 controls the deformation. Two severe simplifications are commonly made when using Eq. (2) for the nuclear geometry. First, nucleons are considered to be independent of each other. Second, protons and neutrons are treated indistinctly so that they are sampled from the same Woods-Saxon distribution, i.e., with identical values for R_0 and d. Experimental measurements and theoretical calculations ruled out both assumptions, as discussed below.

Since the early 1980s, the tails of the proton (p) and neutron (n) distributions are known to be distinct [31–33], i.e., R_0 and d in Eq. (2) are isospin dependent. The neutron distribution populates the outer region of neutron-rich nuclei. That is, the difference between the neutron and proton distributions

TABLE I. Woods-Saxon parameters for the two isobar collision systems.

Nucleus	R_0 [fm]	d [fm]	β_2
${}^{96}_{40}$Zr	5.02	0.46	0
${}^{96}_{44}$Ru	5.085	0.46	0.158

mean square radii, which can be written as

$$\Delta r_{np} = \langle r_n^2 \rangle^{1/2} - \langle r_p^2 \rangle^{1/2}, \tag{4}$$

is positive. Following the Woods-Saxon parametrization given by Eq. (2), this phenomenon translates into nuclei having either $R_{0,p} < R_{0,n}$, $d_n \sim d_p$, dubbed the *neutron-skin* type, or $R_{0,p} \sim R_{0,n}$, $d_n > d_p$, referred to as *neutron-halo* type. A remarkable example of the latter category is ^{208}Pb with $\Delta r_{np} \sim 0.15$ fm [34]. In this case, the implications of $\Delta r_{np} \neq 0$ in the context of observables relevant for the heavy-ion program at the LHC were recently studied in Refs. [35–38]. Interestingly, one of the nuclei chosen for the isobar run at RHIC, ${}^{96}_{40}$Zr, also pertains to the neutron-halo category with

$$\Delta r_{np}|_{{}^{96}_{40}\mathrm{Zr}} = 0.12 \pm 0.03\,\mathrm{fm} \tag{5}$$

as extracted from the experimental analysis performed with the Low Energy Antiproton Ring at CERN [27,28]. The goal of this work is to study the consequences of considering isospin-dependent Woods-Saxon distributions fulfilling the upper limit of the constraint given by Eq. (5), $\Delta r_{np} = 0.15$ fm, to describe ${}^{96}_{40}$Zr on CME-related observables. Note that we take the upper limit of $\Delta r_{np} = 0.15$ fm with the purpose of studying the neutron-skin impact at its extreme.

For that purpose, the starting points are the experimental values for (R_0, d) of the charge distribution [39], displayed both for ${}^{96}_{40}$Zr and ${}^{96}_{44}$Ru in Table I. To extract the values of point distributions $(R_{0,p(n)}, d_{p(n)})$ from the charged ones, keeping the size of the nucleus fixed, we follow the procedure outlined in Refs. [37,40,41]. It is not the goal of this paper to repeat the precise derivation detailed in the aforementioned papers. For completeness, in the Appendix we provide the formulas that were used to obtain the values of $(R_{0,p(n)}, d_{p(n)})$ shown in Table II where we observe how $\Delta r_{np} = 0.15$ fm is translated into a larger value of the diffusiveness for the neutron distribution while the radius remains the same for both types of nucleons. The ratio between the one-body densities of neutrons and protons in ${}^{96}_{40}$Zr as function of the radial distance is displayed in Fig. 1. As expected, this ratio remains flat for the Woods-Saxon distribution while the inclusion of the neutron skin enhances the probability of finding a neutron inside the nucleus at large radial distances. Therefore,

TABLE II. Woods-Saxon parameters for the proton and neutron distributions of ${}^{96}_{40}$Zr.

Nucleon in ${}^{96}_{40}$Zr	R_0 [fm]	d [fm]
p	5.08	0.34
n	5.08	0.46

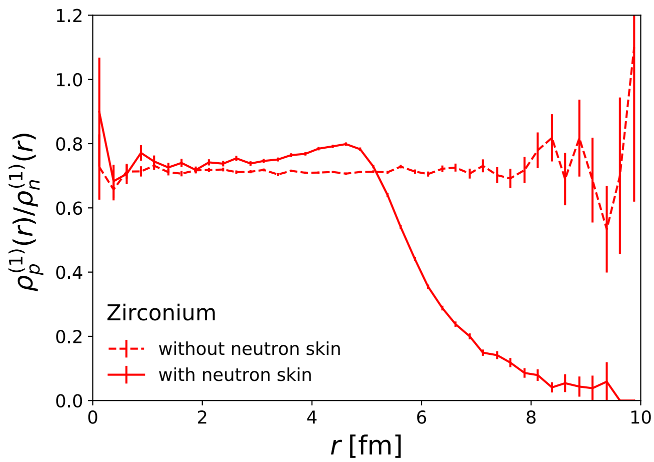

FIG. 1. Ratio of one-body density of protons to neutrons as a function of the radial distance for $^{96}_{40}$Zr with (solid) or without (dashed) considering the neutron-skin effect. Error bars account for statistical uncertainties.

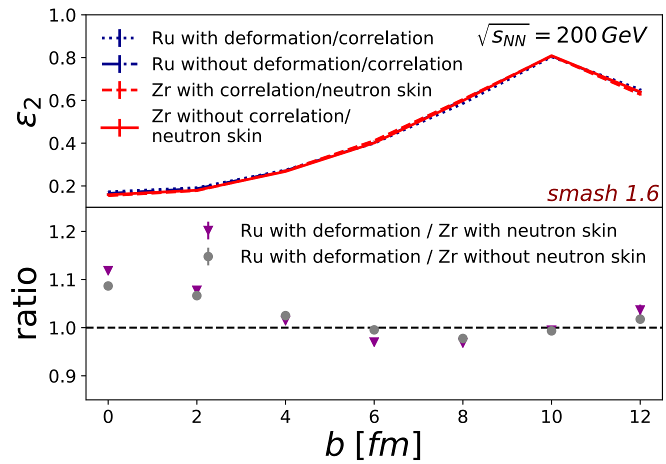

FIG. 2. Top: Participant eccentricity [see Eq. (6)] as a function of the impact parameter for $^{96}_{40}$Zr (red) with (solid) and without (dashed) neutron skin and for $^{96}_{44}$Ru (blue) with (solid) and without (dashed) deformation. Bottom: Effect of the neutron skin on the eccentricity ratio between $^{96}_{44}$Ru and $^{96}_{40}$Zr.

peripheral $^{96}_{40}$Zr + $^{96}_{40}$Zr collisions are expected to be dominated by neutron-neutron interactions. One further comment is in order before addressing the role of nucleon-nucleon (NN) short-range correlations (SRC). The nuclear structure of $^{96}_{40}$Zr and $^{96}_{44}$Ru differ not only because of the neutron skin but also due to the deformation of the latter as exposed in Table I. Although there are some studies (e.g., Ref. [42]) that indicate the opposite situation, i.e., $^{96}_{40}$Zr is deformed while $^{96}_{44}$Ru is not, we stick to the former scenario in order to isolate the impact of deformation from the neutron skin. The deformation affects the geometry of the nucleus in such a way that it has an ellipsoidal shape. In each event, the deformed nuclei are rotated by an arbitrary angle before the collision to reflect the experimental situation in a realistic fashion.

An accurate description of the colliding nuclei, along with neutron skin, calls for inclusion of NN correlations in the ground state [43], which are expected to play a role in different nuclear phenomena [44,45]. A signature of SRC correlations in coordinate space is a peculiar short-range structure [46]. A full *ab initio* theoretical description of the nuclear many-body wave function for large nuclei is an outstanding challenge.

To account for NN SRC in complex nuclei, Alvioli *et al.* [47] proposed a METROPOLIS Monte Carlo generator of nuclear configurations. The method uses an approximate wave function, including spatial and spin-isospin dependence, as a probability measure of nucleon positions. Configurations can implement neutron skin, provided a parametrization of the neutron and proton profiles is known [38], as in here.

SMASH. To demonstrate the effects of the deformation of $^{96}_{44}$Ru and the neutron skin of $^{96}_{40}$Zr in nuclear collisions, the hadronic transport approach SMASH is employed. As a reference to the calculations employing the sophisticated spatial distributions explained in the previous section, the default Woods-Saxon initialization as described in Ref. [29] is used. In SMASH, all well-established particles from the PDG 2018 [48] data are included. Apart from the initialization, isospin symmetry is assumed, meaning that the masses of isospin partners are assumed to be equal as well as their interactions are identical. The collision criterion is realized in a geometric way. The initial binary interactions of nucleons at high $\sqrt{s}$ proceed mainly via string excitation and decay [49]. For all calculations, SMASH-1.6 has been used [50].

Background: Eccentricity. The experimentally measured flow harmonics characterizing the azimuthal distribution of hadrons are an imprint of the QGP evolution acting on the initial spatial anisotropy of the nuclear overlap region. The latter is commonly characterized by the participant eccentricity defined, on an event-by-event basis, by

$$\varepsilon_2 = \frac{\sqrt{(\sigma_y - \sigma_x)^2 + 4\sigma_{xy}^2}}{\sigma_x^2 + \sigma_y^2}, \tag{6}$$

where $\sigma_x^2 = \langle x^2 \rangle - \langle x \rangle^2$ and $\sigma_{xy} = \langle xy \rangle - \langle x \rangle \langle y \rangle$. Finally, $\langle \cdot \rangle$ denotes the average over all participants in one event. In Fig. 2, we show the eccentricity as a function of the collision's impact parameter. We show results for the time where corresponding to the two nuclei completely overlapping, estimated in a geometric way as

$$t = R/(\sqrt{\gamma^2 - 1}), \tag{7}$$

where R is the nuclear radius and γ is the Lorentz factor.

We confirm that the impact of nucleon-nucleon correlations on ε_2 is negligible as demonstrated in Ref. [51], where correlations were shown to affect the fluctuations of flow harmonics. Further, ε_2 is shown to be resilient to the neutron skin effect (solid versus dashed red lines in Fig. 2 and bottom panel). This results from the fact that the neutron skin does not modify the global shape of the nucleus; i.e., the size of the nucleus remains identical with or without it. In turn, when focusing on the ratio of ε_2's between the two isobar systems (Fig. 2, bottom panel), we observe up to a 10% difference in ultracentral collisions. This effect persists down to midcentral collisions, i.e., $b = 4$ fm and it is not caused

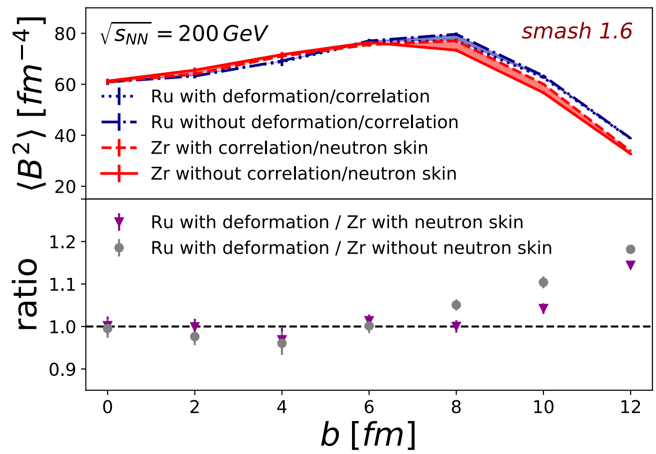

FIG. 3. Top: Strength of magnetic field [see Eq. (8)] squared for ${}^{96}_{40}$Zr (red) with (solid) and without (dashed) neutron skin and for ${}^{96}_{44}$Ru (blue) with (dotted) and without (dash-dotted) deformation. Bottom: Effect of the neutron skin on the magnetic field strength squared ratio between ${}^{96}_{44}$Ru and ${}^{96}_{40}$Zr.

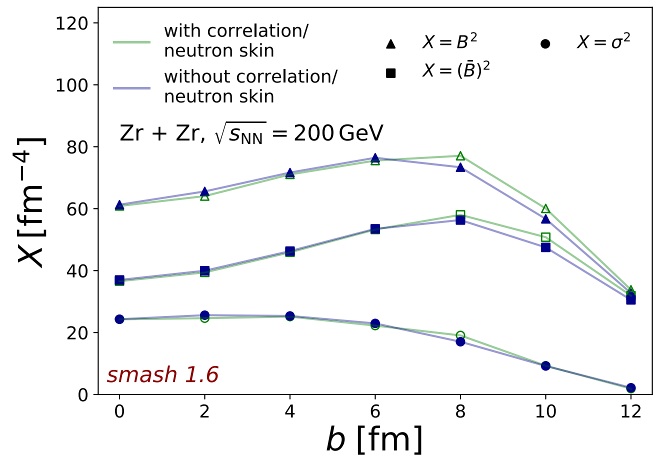

FIG. 4. Statistical properties of the magnetic field distribution, absolute value squared (triangles), mean (squares), and variance (circles), as a function of the impact parameter in ${}^{96}_{40}$Zr + ${}^{96}_{40}$Zr collisions with (green line) and without (blue line) neutron skin.

by either the neutron skin or the NN SRC. We pinpoint the deformation to be the source of this enhancement. This result at the eccentricity level is in quantitative agreement with the v_2 values shown in Ref. [25]. Therefore, we suggest to only consider collisions with $b > 6$ fm (to be translated into the experiment's centrality definition) in order to ensure an identical background component on the isobar run.

Signal: Magnetic field strength. Strong magnetic fields are essential to convert the chiral imbalance [see Eq. (1)] into a discernible charge separation in the particles that reach the detector. Like previous works in the literature [52,53], we compute the magnetic field in the framework of Lienard-Wiechert potentials [54,55], i.e.,

$$e\vec{B}(t,\vec{r}) = \alpha \sum_{i=1}^{N_{ch}} \frac{(1 - v_i^2)(\vec{v}_i \times \vec{R}_i)}{R_i^3\left[1 - (\vec{R}_i \times \vec{v}_i)^2/R_i^2\right]^{3/2}}, \qquad (8)$$

where the sum runs over all charged particles N_{ch}, $\vec{v}$ is the velocity of each particle, and $\vec{R}_i = \vec{r} - \vec{r}_i(t)$. In the last expression, $\vec{r}$ is the observation point and $\vec{r}_i$ is the position of the ith charged particle. We compute the magnetic field at the time where it is maximal, given by Eq. (7), and at the central point $\vec{r} = 0$. To avoid singularities when $\vec{R}_i \to 0$, we do not include particles with $R_i < 0.3$ fm in Eq. (8).

Figure 3 shows the event-average magnetic field strength squared, $\langle B^2 \rangle$, as a function of the impact parameter. Notice that, for completeness, in the top panel, we show the effect of deformation on the magnetic field in the ${}^{96}_{44}$Ru case. We refrain from comparing this option with ${}^{96}_{40}$Zr as there are neither experimental indications nor theoretical predictions that suggest both nuclei to be undeformed. Therefore, in the bottom panel of Fig. 3 we display the ratio between the two systems in a realistic scenario, i.e., considering deformation for ${}^{96}_{44}$Ru and focusing on the role of the neutron skin on the ${}^{96}_{40}$Zr case. We find that the inclusion of the neutron skin on the description of ${}^{96}_{40}$Zr's nuclear structure counterbalances the excess of protons in ${}^{96}_{44}$Ru and leads to a magnetic field strength ratio close to one up to $b \sim 8$ fm. We observe a sizable difference on the magnetic field generated by both systems only arises when going to ultraperipheral collisions ($b > 12$ fm). This is the main result of this work that can be naturally interpreted as follows. The neutron skin, as shown in Fig. 1, enhances the number of neutron-neutron interactions in peripheral collisions or, equivalently, the concentration of protons in the central point that contribute to Eq. (8), leading to a larger B field. Consequently, our study pushes the centrality cut needed to select the events where the CME search were to be performed to significantly larger values.

To better understand the origin of the magnetic field enhancement when the neutron skin is included in ${}^{96}_{40}$Zr, we study the mean ($\langle B \rangle$), the variance (σ^2), and the magnetic field squared (B^2) as a function of the impact parameter. These three quantities are related by

$$B^2 = \langle B \rangle^2 + \sigma^2 . \qquad (9)$$

The results are shown in Fig. 4. Interestingly, in the range where the enhancement of the magnetic field is observed in Fig. 3, i.e., $b \gtrsim 8$ fm, the mean increases when the neutron skin is taken into account whereas the variance stays constant. This indicates an increased magnetic field on average and not as a result of a larger degree of fluctuations.

Summary. We investigated the influence of an experimentally measured feature of ${}^{96}_{40}$Zr, namely, the neutron-skin effect on observables related to CME searches with the isobar program at RHIC. The main results of this work can be summarized as follows:

(1) The background component, namely azimuthal correlations arising from flow, is expected to be $O(10\%)$ larger in ${}^{96}_{44}$Ru + ${}^{96}_{44}$Ru than in ${}^{96}_{40}$Zr + ${}^{96}_{40}$Zr in ultracentral collisions.
(2) The difference between the magnetic field strength generated in both collision systems is reduced by half when including the neutron skin effect in the description of ${}^{96}_{40}$Zr.

Therefore, we conclude that details of the nuclear spatial distributions need to be accounted for in a meaningful interpretation of the experimental measurements related to the CME effect in the isobar run.

Acknowledgments. We would like to express our gratitude to Niklas Mueller, Vladimir Skokov, and Pritwish Tribedy for helpful discussions during the realization of this work. M.A. acknowledges a CINECA award under the ISCRA initiative for making high-performance computing resources available. H.E. and J.H. acknowledge support by the Helmholtz International Center for the Facility for Antiproton and Ion Research (HIC for FAIR) within the framework of the Landes-Offensive zur Entwicklung Wissenschaftlich-Oekonomischer Exzellenz (LOEWE) program from the State of Hesse. This project was further supported by the DAAD funded by BMBF with Project No. 57314610 and by the Deutsche Forschungsgemeinschaft (DFG) through Grant No. CRC-TR 211, Strong interaction matter under extreme conditions. A.S.O.'s work was supported by the U.S. Department of Energy, Office of Science, Office of Nuclear Physics, under Contract No. DE-SC0012704, and by Laboratory Directed Research and Development (LDRD) funds from Brookhaven Science Associates. The research of M.S. was supported by the U.S. Department of Energy, Office of Science, Office of Nuclear Physics, under Award No. DE-FG02-93ER40771. Computing resources provided by the GOETHE-CSC are acknowledged as well.

APPENDIX

In order to transform the charge distribution to pointlike distributions of protons and neutrons, we follow several steps based on Refs. [40,41,56]. First, we obtain the mean square charge distribution radius by using

$$\langle r_{\rm ch}^2\rangle = \frac{3R_0^2}{5}\left(1+\frac{7\pi^2 d^2}{3R_0^2}\right). \tag{A1}$$

Next, the value of $\langle r_p^2\rangle$ is obtained by unfolding, i.e.,

$$\langle r_{\rm ch}^2\rangle = \langle r_{\rm p}^2\rangle + R_p^2, \tag{A2}$$

where the radius of the proton is $R_p = 0.875$ fm. After finding the value of $\langle r_{\rm p}^2\rangle$, one can calculate $R_{0,p}$ and d_p as follows:

$$R_{0,p} = R_0 + \frac{5R_0\langle r_p^2\rangle}{7\pi^2 d^2 + 15R_0^2}, \tag{A3}$$

$$d_p^2 = d^2 - \frac{5\langle r_p^2\rangle\left(d^2 + 3R_0^2/\pi^2\right)}{7\pi^2 d^2 + 15R_0^2}. \tag{A4}$$

Once the Woods-Saxon parameters for the proton distribution are known, and in the case of a neutron-halo type ($R_{0,p} = R_{0,n}$), the only missing parameter is the diffusiveness of the neutron distribution. To find it, one has to replace $\langle r_p^2\rangle$ in Eq. (A4) by $(\Delta r_{np} + \langle r_p^2\rangle^{1/2})^2$.

This procedure leads to the values quoted in Table II that ensure the nucleus size to be identical when considering pointlike or charge distributions.

[1] Q. Li, D. E. Kharzeev, C. Zhang, Y. Huang, I. Pletikosić, A. V. Fedorov, R. D. Zhong, J. A. Schneeloch, G. D. Gu, and T. Valla, Nat. Phys. **12**, 550 (2016).
[2] T. Lappi and L. McLerran, Nucl. Phys. A **772**, 200 (2006).
[3] T. Lappi and S. Schlichting, Phys. Rev. D **97**, 034034 (2018).
[4] P. Guerrero-Rodríguez, J. High Energy Phys. 08 (2019) 026.
[5] F. R. Klinkhamer and N. S. Manton, Phys. Rev. D **30**, 2212 (1984).
[6] M. Mace, S. Schlichting, and R. Venugopalan, Phys. Rev. D **93**, 074036 (2016).
[7] M. Mace, N. Mueller, S. Schlichting, and S. Sharma, Phys. Rev. D **95**, 036023 (2017).
[8] E. Stewart and K. Tuchin, Phys. Rev. C **97**, 044906 (2018).
[9] G. Inghirami, M. Mace, Y. Hirono, L. Del Zanna, D. E. Kharzeev, and M. Bleicher, Eur. Phys. J. C **80**, 293 (2020).
[10] K. Fukushima, D. E. Kharzeev, and H. J. Warringa, Phys. Rev. D **78**, 074033 (2008).
[11] A. Bzdak, V. Koch, and J. Liao, Lect. Notes Phys. **871**, 503 (2013).
[12] S. A. Voloshin, Phys. Rev. C **70**, 057901 (2004).
[13] B. I. Abelev *et al.* (STAR Collaboration), Phys. Rev. Lett. **103**, 251601 (2009).
[14] J. Adam *et al.* (STAR Collaboration), Phys. Lett. B **798**, 134975 (2019).
[15] B. I. Abelev *et al.* (STAR Collaboration), Phys. Rev. C **81**, 054908 (2010).
[16] L. Adamczyk *et al.* (STAR Collaboration), Phys. Rev. Lett. **113**, 052302 (2014).
[17] V. Khachatryan *et al.* (CMS Collaboration), Phys. Rev. Lett. **118**, 122301 (2017).
[18] B. Abelev *et al.* (ALICE Collaboration), Phys. Rev. Lett. **110**, 012301 (2013).
[19] A. Bzdak, V. Koch, and J. Liao, Phys. Rev. C **83**, 014905 (2011).
[20] S. Schlichting and S. Pratt, Phys. Rev. C **83**, 014913 (2011).
[21] N. Magdy, S. Shi, J. Liao, N. Ajitanand, and R. A. Lacey, Phys. Rev. C **97**, 061901(R) (2018).
[22] V. Koch, S. Schlichting, V. Skokov, P. Sorensen, J. Thomas, S. Voloshin, G. Wang, and H.-U. Yee, Chin. Phys. C **41**, 072001 (2017).
[23] W.-T. Deng, X.-G. Huang, G.-L. Ma, and G. Wang, Phys. Rev. C **97**, 044901 (2018).
[24] X.-L. Zhao, G.-L. Ma, and Y.-G. Ma, Phys. Rev. C **99**, 034903 (2019).
[25] B. Schenke, C. Shen, and P. Tribedy, Phys. Rev. C **99**, 044908 (2019).
[26] H.-J. Xu, X. Wang, H. Li, J. Zhao, Z.-W. Lin, C. Shen, and F. Wang, Phys. Rev. Lett. **121**, 022301 (2018).
[27] A. Trzcinska, J. Jastrzebski, P. Lubinski, F. J. Hartmann, R. Schmidt, T. von Egidy, and B. Klos, Phys. Rev. Lett. **87**, 082501 (2001).
[28] A. Trzcinska, J. Jastrzebski, P. Lubinski, F. J. Hartmann, R. Schmidt, T. von Egidy, and B. Klos, Nucl. Instrum. Meth. B **214**, 157 (2004).
[29] J. Weil *et al.*, Phys. Rev. C **94**, 054905 (2016).
[30] R. D. Woods and D. S. Saxon, Phys. Rev. **95**, 577 (1954).

[31] A. Chaumeaux, V. Layly, and R. Schaeffer, Ann. Phys. **116**, 247 (1978).
[32] C. J. Horowitz, K. S. Kumar, and R. Michaels, Eur. Phys. J. A **50**, 48 (2014).
[33] G. Hagen *et al.*, Nat. Phys. **12**, 186 (2015).
[34] C. M. Tarbert *et al.*, Phys. Rev. Lett. **112**, 242502 (2014).
[35] I. Helenius, H. Paukkunen, and K. J. Eskola, Eur. Phys. J. C **77**, 148 (2017).
[36] H. Paukkunen, Phys. Lett. B **745**, 73 (2015).
[37] C. Loizides, J. Kamin, and D. d'Enterria, Phys. Rev. C **97**, 054910 (2018); **99**, 019901(E) (2019).
[38] M. Alvioli and M. Strikman, Phys. Rev. C **100**, 024912 (2019).
[39] B. Pritychenko, M. Birch, B. Singh, and M. Horoi, At. Data Nucl. Data Tables **107**, 1 (2016); **114**, 371(E) (2017).
[40] J. D. Patterson and R. J. Peterson, Nucl. Phys. A **717**, 235 (2003).
[41] M. Warda, X. Vinas, X. Roca-Maza, and M. Centelles, Phys. Rev. C **81**, 054309 (2010).
[42] P. Möller, A. J. Sierk, T. Ichikawa, and H. Sagawa, At. Data Nucl. Data Tables **109–110**, 1 (2016).
[43] M. Duer *et al.* (CLAS Collaboration), Phys. Rev. Lett. **122**, 172502 (2019).
[44] M. Alvioli, C. Ciofi degli Atti, I. Marchino, V. Palli, and H. Morita, Phys. Rev. C **78**, 031601(R) (2008).
[45] M. Alvioli, C. Ciofi degli Atti, B. Z. Kopeliovich, I. K. Potashnikova, and I. Schmidt, Phys. Rev. C **81**, 025204 (2010).
[46] M. Alvioli, C. Ciofi Degli Atti, L. P. Kaptari, C. B. Mezzetti, and H. Morita, Int. J. Mod. Phys. E **22**, 1330021 (2013).
[47] M. Alvioli, H. J. Drescher, and M. Strikman, Phys. Lett. B **680**, 225 (2009).
[48] M. Tanabashi *et al.* (Particle Data Group), Phys. Rev. D **98**, 030001 (2018).
[49] J. Mohs, S. Ryu, and H. Elfner, J. Phys. G **47**, 065101 (2020).
[50] D. Oliinychenko, V. Steinberg, J. Weil, M. Kretz, H. E. Petersen, J. Staudenmaier, S. Ryu, A. Schäfer, J. Rothermel, J. Mohs, F. Li, L. Pang, D. Mitrovic, A. Goldschmidt, L. Geiger, L. Prinz, J.-B. Rose, and J. Hammelmann, smash-transport/smash: Smash-1.6, 2019, https://zenodo.org/record/3485108#.XvCXoS2B124.
[51] M. Alvioli, H. Holopainen, K. J. Eskola, and M. Strikman, Phys. Rev. C **85**, 034902 (2012).
[52] A. Bzdak and V. Skokov, Phys. Lett. B **710**, 171 (2012).
[53] V. Skokov, A. Yu. Illarionov, and V. Toneev, Int. J. Mod. Phys. A **24**, 5925 (2009).
[54] A. Lienard, L' Éclairage Électrique **16**, 5 (1898).
[55] E. Wiechert, Ann. Phys. **309**, 667 (1901).
[56] L. L. Salcedo, E. Oset, M. J. Vicente-Vacas, and C. Garcia-Recio, Nucl. Phys. A **484**, 557 (1988).